Received: 28 August 2024 | Revised: 28 December 2024 | Accepted: 3 February 2025

DOI: 10.1002/pc.29656

RESEARCH ARTICLE

Polymer COMPOSITES WILEY

Mechanical properties of novel uniform/gradient auxetic structures made of CFRP composites

Zhen-Yu Li[1] | **Wei-Jing Wang**[2] | **Hong-Ze Li**[3] | **Jin-Shui Yang**[3] | **Wei-Ming Zhang**[2] | **Xin-Tao Wang**[4] | **Jian Xiong**[2] | **Hong Hu**[1]

[1]School of Fashion and Textiles, The Hong Kong Polytechnic University, Kowloon, China

[2]Center for Composite Materials, Harbin Institute of Technology, Harbin, China

[3]Qingdao Innovation and Development Base, Harbin Engineering University, Qingdao, People's Republic of China

[4]Key Laboratory of Advanced Ship Materials and Mechanics, College of Aerospace and Civil Engineering, Harbin Engineering University, Harbin, People's Republic of China

Correspondence
Hong Hu, School of Fashion and Textiles, The Hong Kong Polytechnic University, Hung Hom, Kowloon, Hong Kong, China.
Email: hu.hong@polyu.edu.hk

Funding information
Research Grants Council of Hong Kong Special Administrative Region Government for the NSFC/RGC Joint Research Scheme, Grant/Award Numbers: N_PolyU516/20, 12061160461

Abstract

Carbon fiber reinforced polymer (CFRP) auxetic composite structures have attracted an increasing attention in recent years due to their lightweight and superior mechanical properties compared with traditional auxetic structures. However, most of the reported all-CFRP auxetic structures are often accompanied with cliff-like stress drops during the failure process, resulting in lower energy absorption. This paper reports the design, fabrication and characterization of a novel type of all-CFRP petal-like auxetic structures with lightweight, high-strength, and good energy absorptive properties. Four uniform/gradient petal-like structures were first made with different angle values and continuous CFRP composites. Then, their mechanical properties, Poisson's ratio and failure mechanism under quasi-static compression loading were analyzed. Based on the quasi-static experimental results, the gradient structure constructed with different cells of varying angles was further selected to study its dynamic response under different initial impact energies and impact positions. The results show that the novel petal-like structures made of continuous CFRP composites can maintain good auxetic properties even under large deformation. Impressively, these structures exhibit a stress plateau phase during compression, indicative of exceptional energy absorption capabilities. The results of low velocity point impact tests also show that the displacement of the initial peak and the number of peaks in the load–displacement curves are significantly influenced by changes in impact position and energy. This research offers a valuable insight into developing and fabricating all-CFRP auxetic structures with superior energy absorption characteristics.

Highlights

- Auxetic structures with high EA capacity are designed and fabricated.
- Their mechanical properties under static and dynamic loads are studied.
- The position and energy of impact have a significant impact on performance.
- The all-CFRP auxetic structure exhibits abundant failure forms.

KEYWORDS

auxetic, damage modes, impact response, low velocity impact, negative poisson's ratio, uniform/gradient structure

1 | INTRODUCTION

Since the groundbreaking work by Lake et al.[1] in preparing negative Poisson's ratio (NPR) foam through thermomechanical method, there has been a significant surge in research efforts focused on exploring the unique physical and mechanical properties of this type of nonconventional mechanical metamaterials. The discovery of NPR structures, commonly referred to as auxetic structures, has catalyzed advancements in the field and led to the development of various representative designs such as re-entrant honeycomb structure,[2–5] double-arrow structure,[6,7] rotation structure,[8–10] elastic instability structure,[11,12] and chiral/ anti-chiral structure.[13–16] These developments have expanded our understanding of NPR materials and opened up new avenues for the design and engineering of innovative structures with unique mechanical properties. Through theoretical analysis, finite element simulation, and experiment, researchers have demonstrated the exceptional properties of auxetic structures, including enhanced shear resistance,[17–19] indentation resistance,[20,21] vibration and sound absorption,[22–24] and energy absorption capabilities.[25–27] As a result, there is a growing interest in exploiting applications of these auxetic structures in different fields such as vehicle engineering,[28] marine engineering,[29] aerospace,[30–32] protective equipment,[33,34] sensors,[35,36] and beyond.

Nevertheless, the facile deformation of auxetic structures also results in a reduction of their bearing capacity. Consequently, recent research endeavors have been concentrated on enhancing their bearing capacity without compromising their auxetic characteristics. Potential solutions to this challenge involve: (1) reinforcing the structure's bearing capacity through the incorporation of ribs or plates[37–39]; (2) augmenting the mechanical properties of the structures by enhancing the material strength[40,41]; and (3) modifying the deformation mechanism of the structures to ameliorate their mechanical properties.[42]

The modifications outlined above have considerably enhanced the qualitative bearing capacity of the structures. Nevertheless, the incorporation of rods has invariably increased the overall weight of the structures, contradicting the demand for lightweight structures in sectors like aerospace. Consequently, CFRP composites possessing lightweight, high specific strength, and high specific stiffness are being employed in the fabrication of auxetic structures. Ehsan et al.[43] combined the stretching-dominated mechanism with the use of CFRP to prepare lightweight and high-strength auxetic structures. Gao et al.[44] employed CFRP to prepare 3D auxetic lattice structures with high stiffness, lightweight, and obvious NPR effect. Their research could promote the application of 3D auxetic lattice structures. However, it seems that the auxetic structures prepared by using interlock assembly process are suitable for large deformation and impact resistance. Zhang et al.[45] showed that the 3D composite auxetic structure prepared by the interlock assembly process only had NPR characteristics under small strains, and brittle fracture occurs in most of the rods under the impact load. This is a disadvantage for the structures' energy absorption. Therefore, the development of auxetic structures with lightweight and high strength, and at the same time with good energy absorption characteristics is regarded as a research target in the following period. To meet the stated objectives, the utilization of continuous fiber-reinforced composites can be an efficient way in the production of auxetic structures. Wang et al.[46] conducted a study utilizing continuous CFRP to fabricate a 3D double-arrow structure. Similarly, Liu et al.[47] utilized continuous fiber-reinforced composites in the preparation of re-entrant honeycomb structures, while Li et al.[48] explored the use of the same material in the development of a composite origami stack structure. These research findings collectively demonstrate the feasibility of fabricating auxetic structures with a unique combination of attributes, such as lightweight construction, superior strength, and exceptional energy absorption capabilities through the utilization of continuous fiber-reinforced composites. However, it is very difficult to prepare complex auxetic structures using continuous fibers, and the difficulty lies in how to balance the preparation process and the complexity of configuration design. Currently, only a limited number of structures can be fabricated in this manner.[48–53]

This study explores the utilization of lightweight and high-strength continuous CFRP to enhance the mechanical properties of auxetic structures. A novel type of petal-like uniform/gradient auxetic structures with multi-stage deformation capability was first designed using angle as an independent variable and manufactured with continuous CFRP composites for experimental evaluation. Then, their mechanical properties and failure modes under quasi-static compressive loads were systematically

investigated. Based on the quasi-static experimental tests, the gradient structure was further studied to understand its dynamic response, failure characteristics, and energy absorption capabilities under point low velocity impact loads. The paper proceeds to detail the design, fabrication, and experimental setup of the structures in Section 2, followed by a description of the finite element analysis method applied to evaluate the structure's response in Section 3. In Section 4, the mechanical properties of uniform/gradient petal-like structures subjected to quasi-static compressive loads are compared, alongside an examination of the dynamic responses of gradient structures exposed to varying impact energies and impact positions. Finally, the conclusions derived from this study will be summarized in Section 5.

2 | EXPERIMENTAL WORK

2.1 | Structure design and preparation process

In contrast to conventional metal auxetic structures, the fabrication of auxetic structures utilizing continuous CFRP composite necessitates additional considerations, such as ensuring uniformity in fiber orientation and contraction direction during preparation, meticulous mold design, and proper resin distribution at corners. The meticulous design of the structure is crucial to ensuring the successful execution of subsequent steps in the manufacturing process.

In general, auxetic structures made of CFRP composites exhibit a loss of auxetic properties under large strain, while simultaneously experiencing an increase in strength and stiffness as a result of material changes.[44] The utilization of continuous CFRP composites enables significant deformation of the structure before failure; however, the occurrence of a cliff-like stress drop due to fiber fracture greatly affects the energy absorption characteristics of the structure.[54] Therefore, it is imperative to ensure that the structure can withstand loading conditions twice before fiber/matrix failure ensues (that is, after the first failure of the structure, the rest of the structure still has a good bearing capacity). Drawing inspiration from the petal-shaped structure,[55] a novel design approach has been introduced to address the aforementioned challenges.

Figure 1A illustrates the design parameters and preparation procedure of the novel petal-like structure. Considering that, the sharp corner is prone to damage in the compression process,[48] the chamfers are strategically smoothed in the mold design. As depicted in Figure 1A, the geometric characteristics of the structure can be described using the following parameters: the inclination angle of the inclined bar θ, the platform width l_h, the horizontal projection length of the inclined bar l_1 and l_2, unit cell length l_3, the radius of the circular section at the connection between the straight rod and the round rod R, thickness of the sheet t, and the length of the rod in the extension direction b. The values of these parameters selected for this study are listed in Table 1. In contrast to unidirectional prepreg laminates, fabric laminates showenhanced capability in mitigating delamination damage upon exposure to low velocity impact loading.[56] As such, the present study incorporates carbon fiber fabric in the fabrication of petal-like sheets. Utilizing the hot molding process, the petal-like sheets were fabricated following the curing curve of the prepreg material (the mechanical properties of composite laminates were the same as those of Li et al.[48]). Through meticulous cutting, stacking, and bonding processes, three uniform petal-like structures and one graded petal-like structure were successfully manufactured. The corresponding specimen diagrams can be observed in Figure 1B.

2.2 | Quasi-static compression and dynamic impact tests

Quasi-static compression experiments on uniform/gradient petal-like structures were carried out according to the ASTM C365 standards.[46] The tests were conducted at room temperature by using a universal testing machine Instron 4505 equipped with a 50 kN load sensor at a loading speed of 1 mm/min. During the compression test, the deformation process is analyzed by digital image correlation (DIC) software, and the failure form of the structures is recorded by high-resolution cameras. Through the utilization of the universal testing machine, data are gathered for longitudinal displacement U_y and reaction force F_y. By applying the formulas $\sigma_y = F_y/(L_x * L_z)$ and $\varepsilon_y = U_y/L_y$, stress and strain values are calculated, with L_x, L_y, and L_z representing the initial dimensions of the structural element. Subsequently, the equivalent compression modulus of the structure is determined through $E_y = \sigma_y/\varepsilon_y$. The focus of this study lies in analyzing structural deformation through a methodical approach. Based upon the research by Li et al.[54] and Yang et al.,[57] the Poisson's ratio of the structures was calculated by utilizing the relative displacements of the middle points within the single cells, as well as between the upper and lower platens. As shown in Figure 2A, the relative displacement of the central position of the cell under compression is determined by averaging the displacements at specified points (X_1, X_2, X_3, and X_4). Subsequently, the nominal strains in both the X and Y

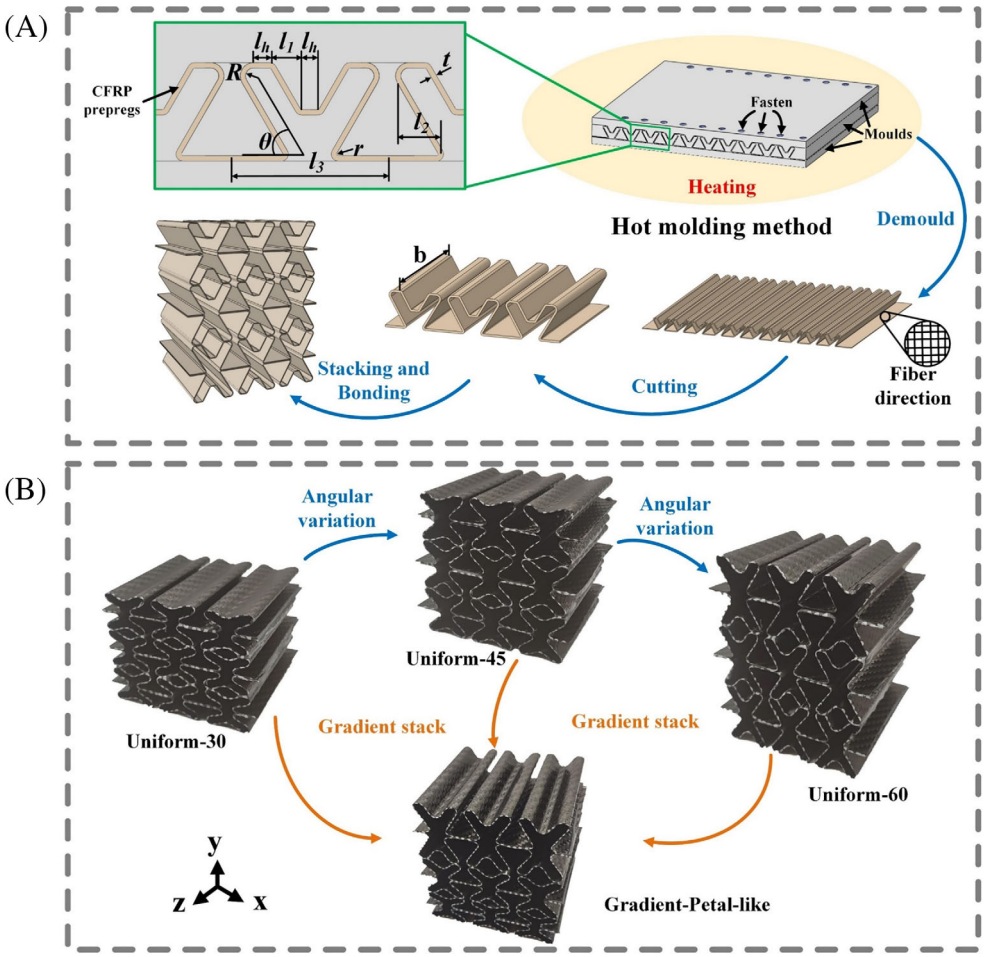

FIGURE 1 (A) Structural design and preparation process. (B) Uniform/gradient peta-like structure specimens.

TABLE 1 Values of geometric parameters used.

t (mm)	l_1 (mm)	l_2 (mm)	l_3 (mm)	l_h (mm)	R (mm)	r (mm)	b (mm)	θ (°)
0.5	6	8	29	3	2	0.55	80	30, 45 or 60

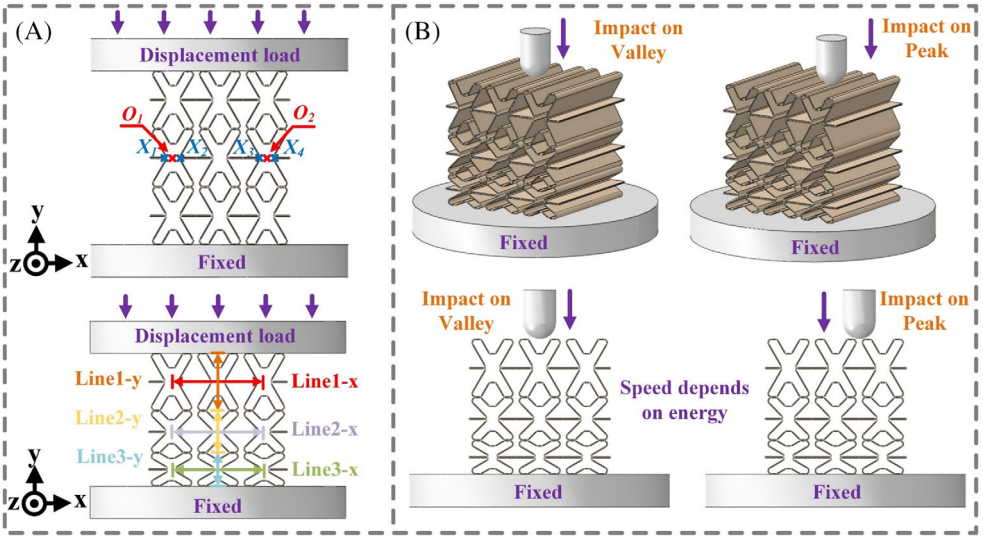

FIGURE 2 Experimental setup. (A) Loading mode under quasi-static compression and reference points for Poisson's ratio calculation. (B) The loading method under the point impacts at different impact positions.

directions are computed, leading to the establishment of the Poisson's ratio for a uniform structure using the equation $\nu_{yx} = -\frac{\varepsilon_x}{\varepsilon_y}$. Furthermore, the study explores the variability in Poisson's ratio within a gradient structure. To address this, the strains in both X and Y directions for each row of the structure were systematically measured.

To study the response of the structure under dynamic impact loading, the Instron CEAST 9350 drop-weight impact test system with a sensor frequency of 106 Hz and a maximum measured load of 90 KN was used to test the gradient petal-like structure according to ASTM D7136M-20.[58] A semi-spherical hammer with a diameter of 20 mm and a mass of 10.4 kg was used to carry out impact experiments on different positions of the gradient petal-like structure with impact energies of 15, 30, and 50 J, respectively. To better study the deformation of the structure under different impact energies, a Mi 14 high-speed camera with an acquisition frequency of 1920 frames/SEC and a resolution of 1280 × 720 pixels is used to record the deformation of the structure. Moreover, an investigation into the effect of impact position on structural impact resistance was carried out. The specific placement of impact positions can be observed in Figure 2B.

3 | NUMERICAL SIMULATION

The ABAQUS/Explicit software was used to systematically investigate the deformation and failure modes of uniform/gradient petal-like structures in quasi-static uniaxial compression. The numerical model comprises three components: the upper and platen, the petal-like structure and the lower palten. The material parameters related to petal-like structures are shown in Appendix A Table A1. The upper and lower platens are represented as rigid bodies, with the displacement controlled by coupled reference points. Following the experimental setup, the lower platen is immobile while the displacement of the upper platen is regulated by a displacement load. The structural analysis employed an eight-node 3D reduced-integration solid element model (C3D8R) with a mesh size of 0.5 mm to optimize computational efficiency while maintaining precision in the results. It is important to note that, to minimize numerical simulation errors, we performed local mesh refinement on the petal-like plates with a thickness of 0.5 mm, ensuring that each layer of prepreg contained at least two mesh elements. Additionally, the results of the mesh convergence analysis are presented in Appendix B Figure A1. Employing hard contact in the nominal direction and frictionless in the tangential direction, along with the vector user material subroutine (VUMAT), which has been proved to be effective in analyzing the deformation and failure mechanisms of composite structures.[59] Therefore, this method was extended in this study.

4 | RESULTS AND DISCUSSION

4.1 | Properties under quasi-static compression

4.1.1 | Compressive response, auxetic characteristic, and failure modes

The equivalent compression modulus and Poisson's ratio of uniform/gradient composite petal-like structures were determined through the methods outlined in Sections 2 and 3, and the obtained results are displayed in Figure 3. It is evident that both the modulus and auxetic effect of the structures increases with increasing angle θ. In the case of the graded petal-like structure, the equivalent compression modulus closely aligns with the average of the three uniform petal-like structures. The presence of cells with smaller angles impedes the lateral contraction of cells with larger angles during compression, thereby diminishing the auxetic characteristics of each layer of cells with the gradient structure relative to the uniform petal-like structures. Notably, a clear relationship was observed between the original auxetic characteristics of the uniform structures and the subsequent reduction in auxetic properties after the introduction of a gradient (Uniform-30 reduced by 22.8%, Uniform-45 reduced by 24.7%, Uniform-60 reduced by 33.7%).

Figure 4 illustrates a comparative analysis of the stress–strain curves and failure modes under quasi-static compression obtained from both the simulation and experiment. The alignment between the simulated and empirical results is notably laudable. At low strain levels, the finite element analyses closely correspond to the experimental observations. Even in instances of structural failure, finite element data exhibit a consistent trend with experimental data. The error is attributed to the fact that the numerical model overlooks the impact of geometric imperfections stemming from the hot molding process. As a result, slight deviations are observed between the stress levels derived from experimentation and predicted by simulation.

It should be noted that petal-like structures composed of continuous CFRP composite exhibit minimal stress fluctuations during the compression process, leading to favorable energy absorption characteristics. The analysis of the failure process diagrams in Figure 4B–E reveals a distinct three-stage progression involving shrink, contact, and rotation. As compression displacement increases,

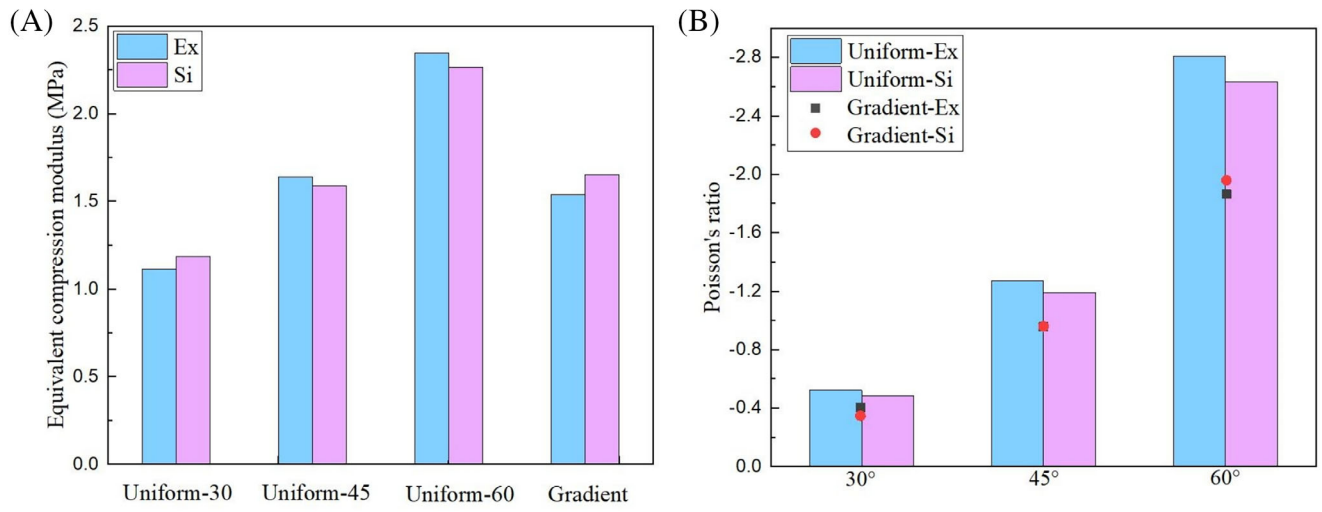

FIGURE 3 Experimental and simulating results for composite petal-like structures with different angles under quasi-static compression loads. (A) Equivalent compression modulus. (B) Poisson's ratio.

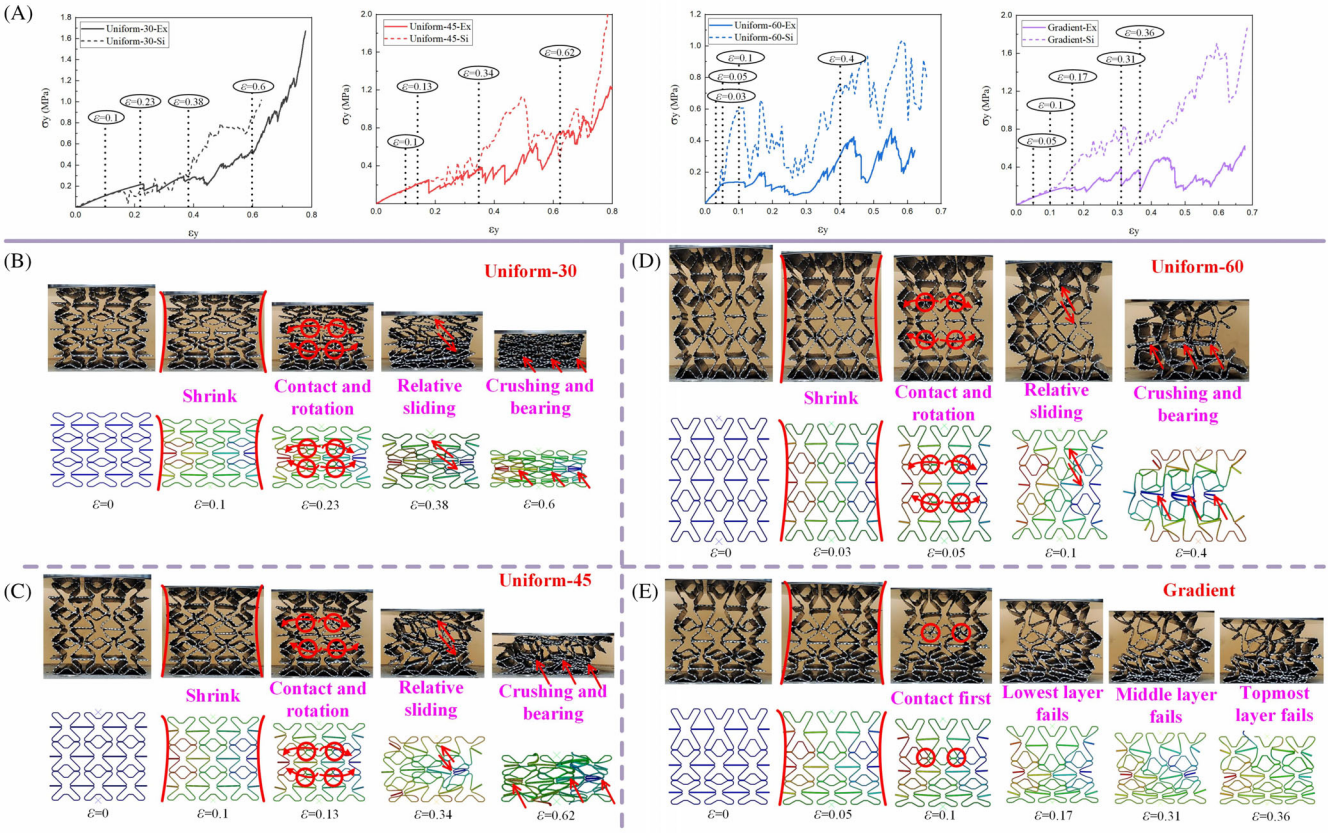

FIGURE 4 Mechanical properties of composite petal-like structures under quasi-static compression loads. (A) Stress–strain curves. (B) Failure mode of Uniform-30 structure. (C) Failure mode of Uniform-45 structure. (D) Failure mode of Uniform-60 structure. (E) Failure mode of Gradient structure.

relative sliding occurs at the semicircular cross-sections in contact, followed by crushing failure at the small chamfer position adjacent to the crossbar. Subsequently, the semicircular sections continue to bear the loads, resulting in a reduced curve fluctuation. The distance between the inclined rod and cross rod plays a critical role in determining stress–strain curve fluctuation upon failure. The structures demonstrate effective energy

absorption characteristics throughout the compression process, even as load fluctuation amplitudes increase with angle value. Increasing angle value enhances the modulus and auxetic properties of the structure, albeit at the expense of strength and increased curve fluctuation intensity. Accordingly, a gradient design approach is proposed and investigated. Examination of Figure 4E highlights the complex failure process of gradient petal-like structures under compression. Notably, 60° cells exhibit enhanced auxetic properties, resulting in their initial contact during compression. The increased modulus of the gradient structure causes the 30° cell layer to fail first, effectively minimizing stress fluctuation before reaching 0.3 strain and enabling high energy absorption characteristics under significant strain.

4.1.2 | Performance comparison

As shown in Figure 5A, the novel composite petal-like structures proposed in this study is compared with other lattice structures[23,60–65] with reference to the Ashby diagram. It is not difficult to find that the new structures proposed in this paper has excellent energy absorption performance at low density. Therefore, the goal of lightweight and high-energy absorption in structural design is realized. The radar chart depicted in Figure 5B illustrates the comprehensive performance evaluation of the uniform/gradient composite petal-like structures outlined in this study (obtained from experimental data). Considering that the Poisson ratio varies among cells within the gradient structure, the average Poisson ratio of the three rows of uniform cells is utilized as the representative Poisson ratio for comparison purposes. The five axes represented in the radar chart correspond to the structure's key properties: lightweight, energy absorption capabilities, auxetic behavior, equivalent compression modulus, and feasibility of manufacturing using continuous CFRP composites. The structures are assessed for their energy absorption characteristics using specific energy absorption (SEA), which measures the amount of energy absorbed per unit volume and density. Despite the unavoidable increase in relative density due to the reduction of angle, all the structures maintain a maximum relative density below 0.15, effectively achieving lightweight construction. Moreover, petal-like structures fabricated with only two layers of fabric prepreg demonstrate favorable energy absorption characteristics, exhibiting an absorption range of 1000-2000 J/kg, surpassing many alternative structures.[66]

Due to limitations in the manufacturing process, structures fabricated with CFRP composite materials often experience a reduction in energy absorption characteristics despite their lightweight nature and high-strength properties.[43,44] This results in a restricted applicability of such materials in engineering. Conversely, the novel petal-like structures proposed in this study are fabricated using continuous fiber-reinforced composite material, enabling them to retain pronounced auxetic characteristics even under large deformation, while preserving requisite strength and stiffness. By conducting Poisson's ratio analysis in section 4.1.1 and referring to the radar diagram presented in Figure 5B, our findings indicate that the gradient structure exhibits favorable modulus E and SEA at a lower relative density. Additionally, the structure demonstrates a variety of Poisson

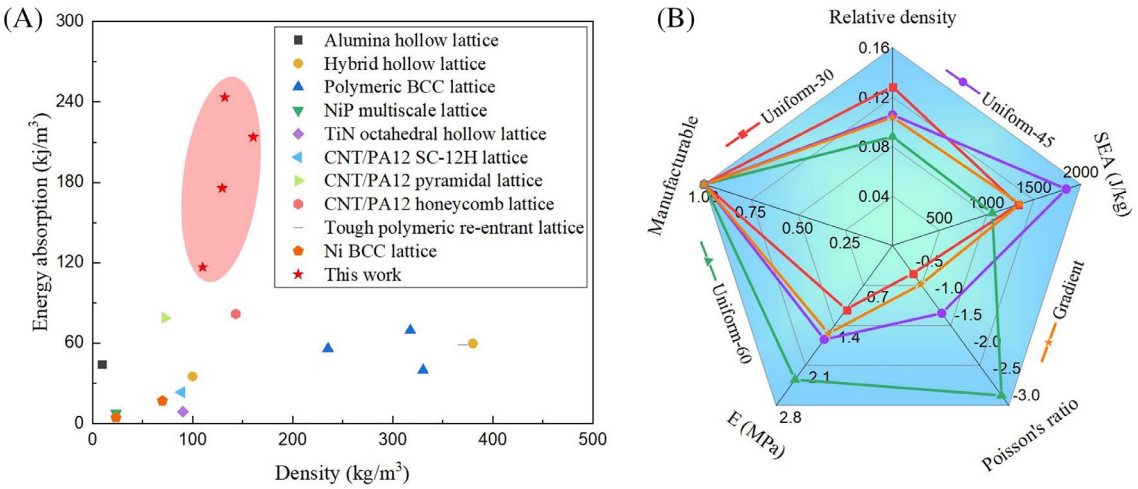

FIGURE 5 Performance analysis. (A) Ashby diagram of energy absorption and density per unit volume. (B) Comprehensive capabilities that combine lightweight, energy absorption properties, Poisson's ratio, equivalent compression modulus, and manufacturability of multifunctional composite petal-like structures.

ratios, suggesting its potential adaptability for diverse engineering requirements. Therefore, further investigations will delve into the mechanical properties and failure mechanisms of gradient petal-like structures under low velocity impact conditions.

4.2 | Properties under low velocity point impact

4.2.1 | Deformation and failure process

For facilitating explanation, the specific designations corresponding to various impact positions and impact energies of the gradient structure presented in Section 2.2 are assigned in Table 2. An examination of the deformation and failure mechanisms of the petal-like structure during impact, as presented in Figure 6, reveals the diverse array of deformation modes of the structure. Unlike the failure progression of the gradient structure under quasi-static compression loading, the cells fail sequentially from the top to the bottom upon exposure to impact loading. In the analysis regarding the energy and impact resistance of the structural configuration, it is observed that the cells located at Line 3 did not experience failure. This discovery indicates that the suggested gradient arrangement successfully shields the fundamental structure from harm when the object requiring protection is located within the cell of the bottom layer.

When subjected to an impact energy of 15j at the "valley" position, the structure exhibits a noticeable contraction pattern. Specifically, the cells located below the impact point undergo a more significant contraction compared to the cells on either side. The increasing contraction of the initial row of cells results in enhanced rotation of the inclined plate within the upper portion of this cell layer. Subsequently, a fracture occurs at the juncture of the diagonal and cross plates. Despite the crushing of the upper portion of the central cell in the first row, the two adjacent cells in the same row continue to tend to contract toward the central position due to the ongoing connection with the lower portion cells. In contrast to the phenomenon observed with the impact "valley" position at 15j energy, the cells located in the second row exhibit a pattern of crushing in response to escalating energy levels. It is noteworthy that upon complete crushing of the middle cell in the first row, the lack of constraint on the adjacent cells results in outward expansion, a visual representation of which can be observed in the final diagrams of Figure 6B,C. Moreover, as the impactor displacement continues to increase, a rotational and relative sliding motion is observed in the lower half of the first row of cells, as well as in the second and third rows. This distinct deformation behavior of the auxetic structure and subsequent structural failure play a pivotal role in enhancing energy dissipation mechanisms.

When the "peak" position of the structure is subjected to an impact load, the structure maintains its auxetic characteristics and exhibits noticeable contact and rotation as depicted in Figure 6D–F. Figure 6D illustrates the deformation caused by the impact of a 15j energy on the "peak" position of the petal-like structure. Upon impact loading, evident contact and rotation are observed in the lower cells of the impactor. Subsequently, the impactor descends further, causing a depression in the inclined plate of the structure. As the impact energy increases, the inclination of the structure toward the impactor becomes more pronounced, and crushing failure is observed in the second layer. Similar to the impact at the "valley" position, once the lower half of the first row of cells under the impactor is completely crushed, the cells lose their constraint and the contraction of both sides ceases.

TABLE 2 Naming of impact tests.

Name	Specimen type	Impact position	Impact energy(J)
Valley-15 J	Gradient	Valley	15
Valley-30 J	Gradient	Valley	30
Valley-50 J	Gradient	Valley	50
Peak-15 J	Gradient	Peak	15
Peak-30 J	Gradient	Peak	30
Peak-50 J	Gradient	Peak	50

4.2.2 | Failure modes of fibers under low velocity impact

In contrast to conventional multicellular structures composed of isotropic materials such as metal or polymer, auxetic structures constructed from continuous CFRP composites exhibit a heightened complexity in terms of failure modes when subjected to low velocity impact loads. This complexity arises from the diverse failure modes inherent in CFRP composites, including fiber stretching, fiber compression, matrix stretching, matrix compression, and interlaminar shear. To accurately characterize the failure mechanisms of these structures, a portable electron microscope with a magnification capability of up to 1600 times (sourced from Shenzhen Tiankui Hardware Tools Co., LTD.) was employed to examine and illustrate the fiber failure, as illustrated in Figure 7.

Upon meticulous examination of the specimen labeled as "Valley-15 J", it is evident that there is no

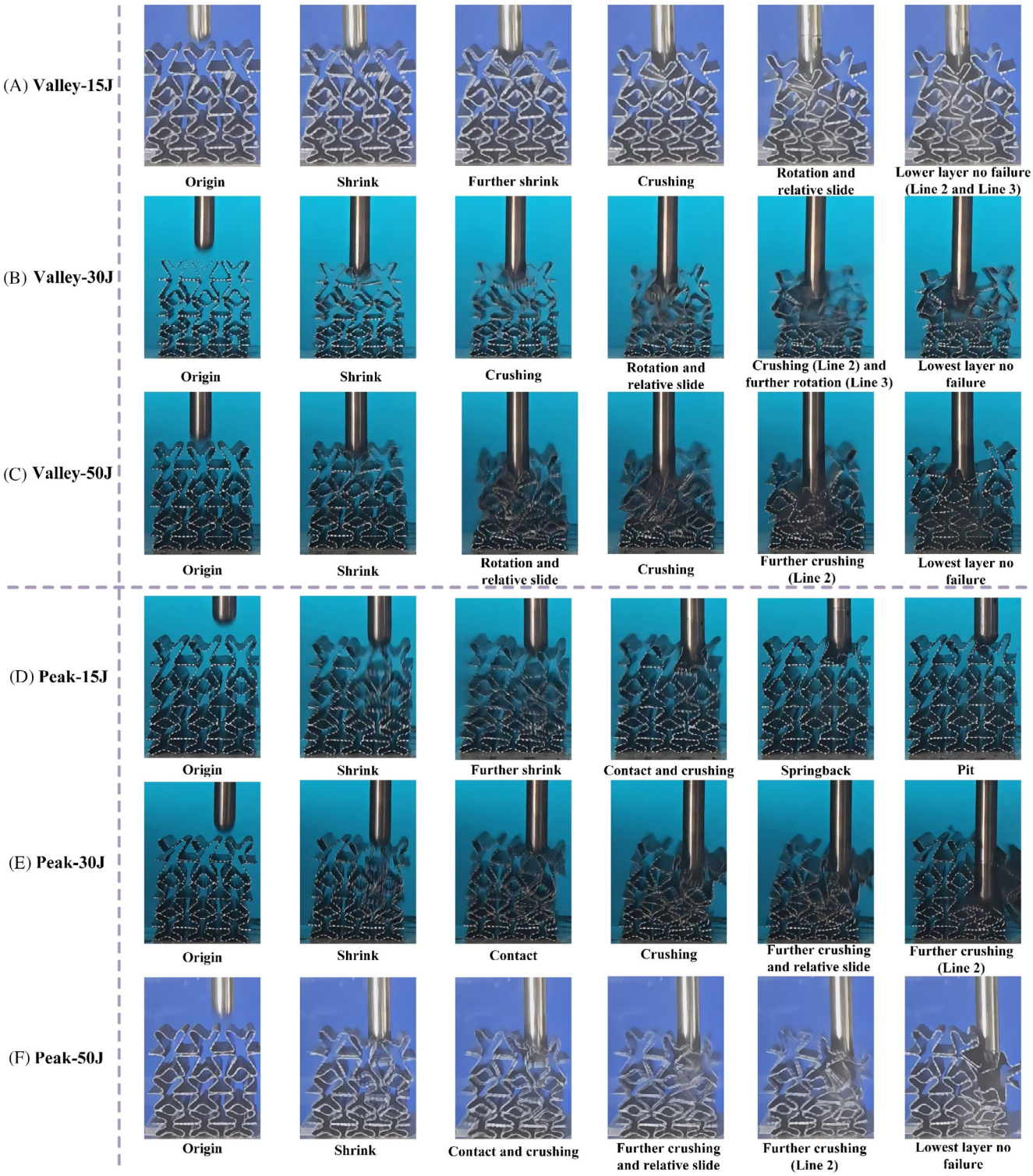

FIGURE 6 Deformation and failure process of gradient specimens under low velocity point impact with different energies. (A) Valley-15 J. (B) Valley-30 J. (C) Valley-50 J. (D) Peak-15 J. (E) Peak-30 J. (F) Peak-50 J.

discernible damage present on the surface. The structural failure is localized at the juncture where the inclined bar meets the horizontal bar. This indicates that the auxetic structure is capable of absorbing impact energy of a minor magnitude (15 J), with the energy being dissipated through deformation and subsequent brittle fracture occurring at the interface between the two mentioned bars. In contrast, the specimen denoted as "Peak-15 J"

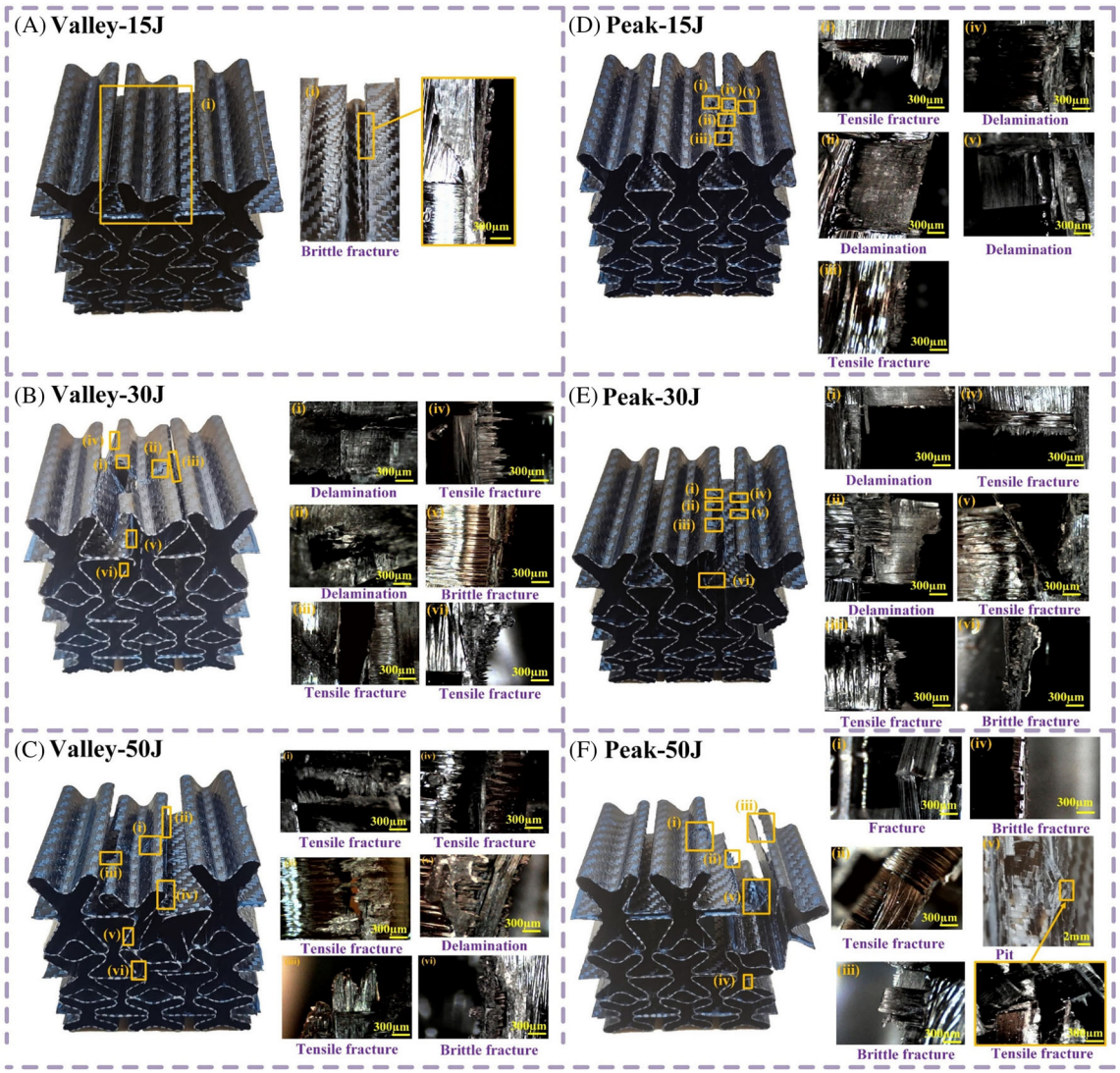

FIGURE 7 Failure forms of the gradient structure under different impact energies and impact positions. (A) Valley-15 J. (B) Valley-30 J. (C) Valley-50 J. (D) Peak-15 J. (E) Peak-30 J. (F) Peak-50 J.

displays a more intricate failure mode of the fibers, characterized by pronounced pits and tears at the impact site, specifically at the connection point between the large semicircular section and the inclined plate. Upon closer inspection of the fibers at the pit and tear locations, it becomes apparent that there is an observable tensile fracture and delamination evident in these areas. Notably, the degree of fiber delamination in the composite petal-like structures formed through fabric preparation remains minimal under low velocity impact loads, consistent with the findings reported by Ma et al.[56] With the escalation of impact energy, the failure mode of fibers exhibits an increasing complexity. Specifically, in the case of "Valley-30 J," significant damages are observed on both sides of the inclined plate, attributed to the auxetic characteristics causing shrinkage toward the center under the impact load. Furthermore, aside from the brittle fractures evident in "Valley-15 J", notable instances of tensile fracture and delamination are observed at pit and tear sites. In the scenario of "Peak-30 J," alongside the presence of pits and tears at lower energy levels, intensified deformation results in excessive deformation at the junction of the inclined plate with the horizontal plate, consequently leading to brittle fracture. At higher impact energy of 50 J, "Valley-50 J" experiences tearing failure at the junction of the semicircular section with the inclined bar, while "Peak-50 J" presents a distinct pit at the maximum displacement of the punch.

4.2.3 | Dynamic response

The force-displacement curves of the composite petal-like gradient structure subjected to hammer impact with

varying impact energies and impact positions were analyzed and presented in Figure 8. Upon examination of the curves for impacts at distinct positions with equal impact energy, it is observed that the impact load has a nearly linear increase up to a falling displacement of 7.5 mm when impacted at the "Valley" position, followed by a "plateau" phase. This phenomenon occurs due to the dynamic response of adjacent cells when the central cell experiences an impact load, resulting in immediate contraction toward the central cell and contact between neighboring cells. The extrusion action of the punch on the inclined plates corresponds closely to the deformation pattern of the cell under compression loading, leading to heightened deformation in the middle cell. As the displacement of the punch is progressively augmented, the semicircular cross-section of the central cell comes into contact with the slanted plates situated on either side, causing a brief slope to rise in the force-displacement curve. Subsequently, as the punch displacement increases, the inclined plates of the two sides cells cease to contact with the central cell, resulting in the absorption of energy through the deformation of the central cell and the manifestation of a plateau on the force-displacement curve. Upon reaching a specific displacement level, the deformation of the upper half of the first layer cell reaches its maximum, leading to fiber failure as the punch continues to descend and the load intensifies.

When hitting the "Peak" position, the punch is equidistantly situated between two cells, thereby exerting an outward extrusion effect on the adjacent cells as it descends. The auxetic properties of the cells also cause them to contract toward the punch's location. Consequently, when impacted at the "Peak" position, the structure exhibits heightened stiffness, resulting in a steeper force-displacement curve. Furthermore, because of cell compression toward the central position and the semicircular section coming into contact with each other, the escalation of punch displacement leads to detrimental effects on the fibers. Consequently, the load exhibits a continuous rise without reaching a "plateau" phase.

When maintaining a constant impact position, the augmentation of impact energy does not significantly affect the initial phase of the force-displacement curves. This suggests that for a specific structure, consistency in impact position results in uniform impact resistance and comparable deformation circumstances, as illustrated in Figure 8D,E. Nonetheless, the escalation of impact energy also results in a greater number of cell failures, as evidenced by a heightened quantity of peaks on the curve.

4.2.4 | Energy absorption and performance comparison

The energy absorption behavior of the novel gradient composite petal-like structure subjected to point impact

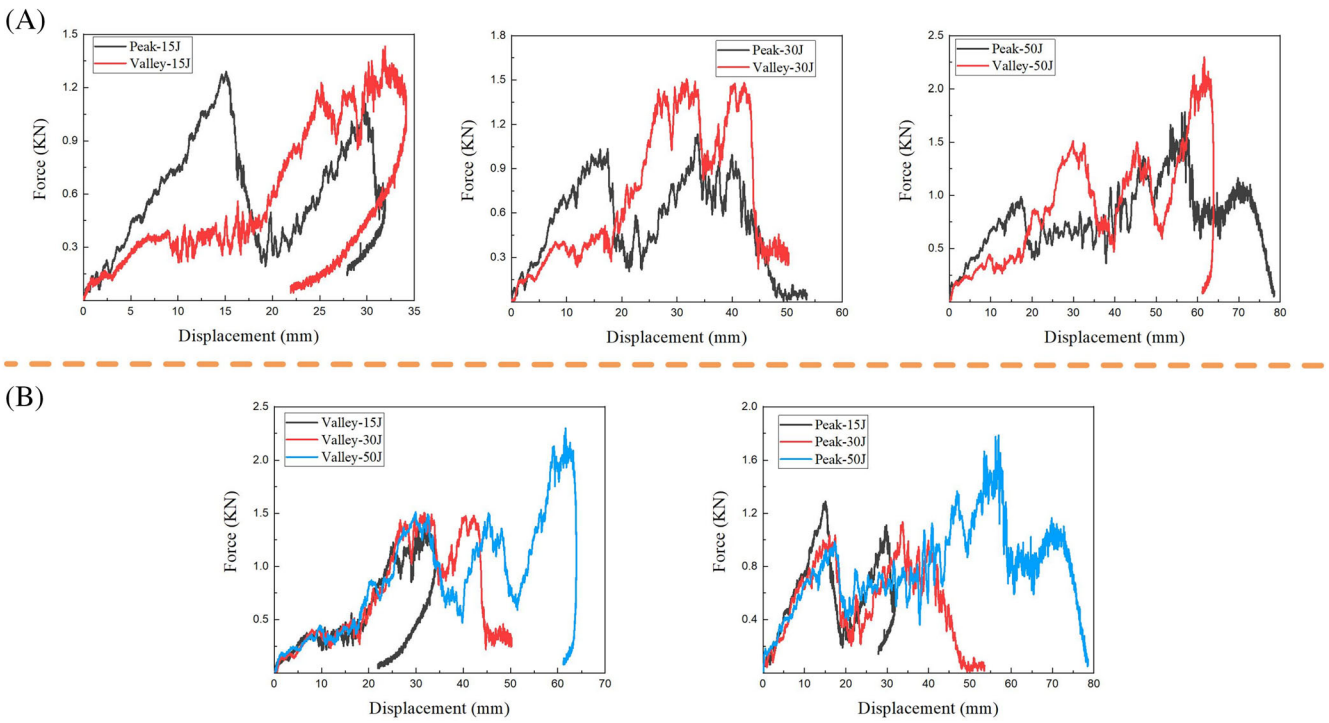

FIGURE 8 Influence of impact energy and impact position on the structural force-displacement curve. (A) Influence of impact position. (B) Influence of impact energy.

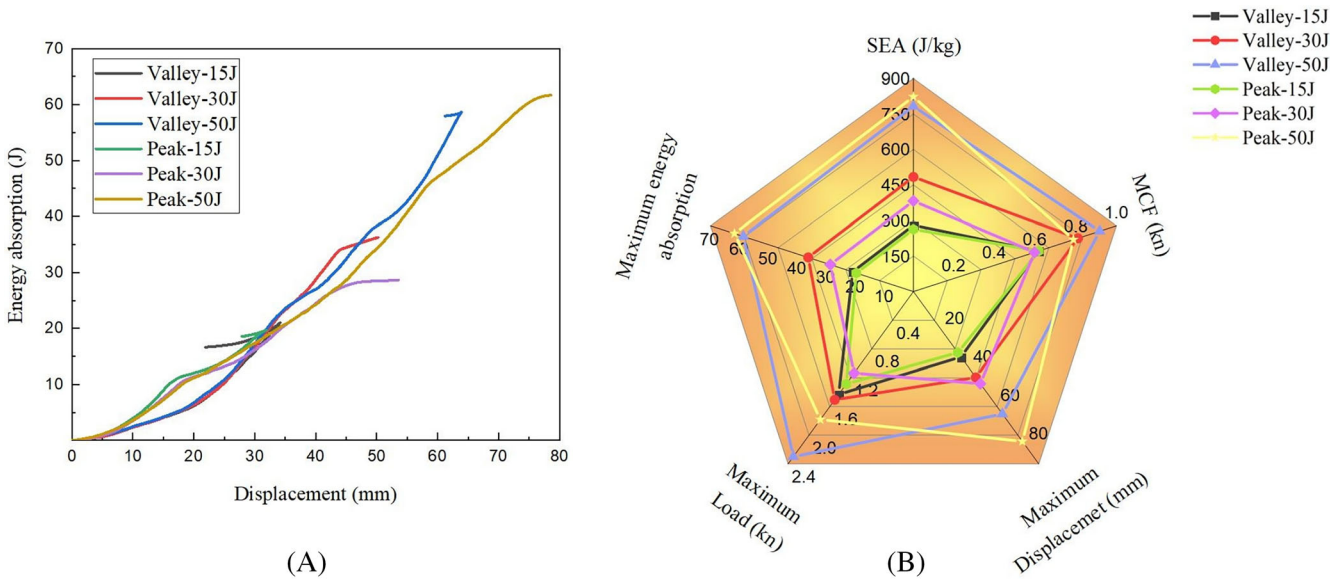

FIGURE 9 Performance comparison of the gradient structure under impact with different locations and energies. (A) Energy absorption-displacement curves. (B) Radar map.

with different locations and energies is illustrated in Figure 9A. It is evident that up to a displacement of 7 mm, varying impact locations exhibit similar energy absorption properties. Subsequently, as the punch displacement increases, the energy absorption behavior of the structure is influenced by the impact location. Notably, at a displacement range of 7–30 mm, the impact "Peak" position demonstrates higher energy absorption capabilities compared to the impact "Valley" position. This observation underscores the ability of fiber destruction to more rapidly dissipate energy than structural deformation.

In the comprehensive analysis of a structure under low velocity impact loads, the mean crush force (MCF) serves as a metric to assess the average load experienced by structures during compression. MCF is determined by the ratio of the energy absorbed by the structure during impact to the displacement of the punch. As shown in Figure 9B, a radar diagram is employed to evaluate five key properties of the structure in question during drop hammer testing: SEA, MCF, Maximum displacement, Maximum load, and Maximum energy absorption. A positive correlation is observed between the initial impact energy and these performance indicators. Notably, the impact "Valley" position results in a higher average load and displacement, while the remaining properties are mainly influenced by the initial impact energy. Impact position has minimal effect on these properties. Additionally, although the impact "Peak" position may exhibit superior energy absorption characteristics with small displacement, the structure's stiffness is compromised due to punch crushing, leading to reduced impact resistance. Consequently, the "Peak" position impact may yield greater maximum displacement.

5 | CONCLUSIONS

Upon evaluation of the deformation process of auxetic structures and the preparation process of continuous CFRP composites, a type of novel uniform/gradient petal-like structures was introduced in the present study. Their compression behavior, auxetic properties, and failure mechanisms under quasi-static compression loads were investigated through simulation and experimental analyses. Subsequently, low velocity impact tests were conducted on the gradient petal-like structure exhibiting favorable overall properties and diverse failure modes, with a systematic exploration of the impact energy and position effects on its mechanical behavior. The main conclusions of the study are as follows: All-CFRP auxetic structures with lightweight, elevated specific strength, heightened specific stiffness, and effective energy absorption capabilities can be designed based on petal-like geometry and manufactured using continuous fiber reinforced composites. Under the quasi-static compression loading, the modulus and auxetic characteristics of the structures increase with increase of angle magnitude, and the gradient design reduces the auxetic characteristics of the structure to a certain extent. The equivalent compression modulus of the gradient structure formed by stacking cells with three angles is approximately equal to the average modulus of the three uniform structures. The quasi-static compression deformation process of the

petal-like structures can be characterized by three distinct stages: shrinkage, contact, and rotation. With the increase of compression displacement, the two adjacent semicircular cross sections are relatively easy to slide, and the position where the inclined sheet and the horizontal sheet are connected is most prone to failure. The gradient structure still has good auxetic characteristics under low velocity point impact and its deformation and mechanical properties are greatly affected by impact location. When impacting at the "Valley" position, the energy of the punch is first dissipated by the structure through the shrinkage, rotation mechanism, and friction between the semicircular cross sections and the plates, and subsequently by the fiber damage. When impacting at the "Peak" position, the adjacent cells contract toward the punch position and the fibers fail to absorb energy rapidly. The impact energy is shown to have minimal influence on the structural deformation and failure modes, but significantly affect the number of damaged cells, as evidenced by the rise in load peak numbers on the force-displacement curve.

FUNDING INFORMATION

This work was supported by the Research Grants Council of Hong Kong Special Administrative Region Government for the NSFC/RGC Joint Research Scheme (Grant Nos: N_PolyU516/20 and No. 12061160461).

DATA AVAILABILITY STATEMENT

The data that support the findings of this study are available from the corresponding author upon reasonable request.

ORCID

Jin-Shui Yang https://orcid.org/0000-0003-1769-0207
Hong Hu https://orcid.org/0000-0002-5098-2415

REFERENCES

1. Lakes RS. Foam structures with a negative Poisson's ratio. *Science*. 1987;235(4792):1038-1040.
2. Šleichrt J, Falta J, Neuhäuserová M, et al. Instrumented dynamic penetration of Sandwich panels with auxetic and non-auxetic Core using direct impact Hopkinson Bar. *Adv Eng Mater*. 2023;25:2300980.
3. Khoa ND, Bohara RP, Ghazlan A, Thai HT, Ngo T. Novel hierarchical bioinspired cellular structures with enhanced energy absorption under uniaxial compression. *Aerosp Sci Technol*. 2024;147:108995.
4. Hung PT, Thai CH, Phung-Van P. Isogeometric free vibration of honeycomb sandwich microplates with the graphene nanoplatelets reinforcement face sheets. *Eng Struct*. 2024;305:117670.
5. Su B, Zhou Z, Qiu J, et al. Multiaxial yield behavior of 2D re-entrant auxetic cellular materials. *Eng Struct*. 2024;311:118216.
6. Guo MF, Yang H, Ma L. 3D lightweight double arrow-head plate-lattice auxetic structures with enhanced stiffness and energy absorption performance. *Compos Struct*. 2022;290:115484.
7. Qu Y, Chen J, Jiao L, Ye T, Hu X. Experiment and finite element analysis of protective honeycombs based on equivalent method for ocean engineering under impact loading. *Compos Struct*. 2024;331:117858.
8. Gupta V, Singh G, Chanda A. Modeling of metamaterial based incision patterns for generating high expansions in skin grafts. *Clin Biomech Bristol Avon*. 2023;110:106118.
9. Hao J, Han D, Zhang XG, et al. A novel compression-torsion coupling metamaterial with tunable Poisson's ratio. *Construct Build Mater*. 2023;395:132276.
10. Huo RY, Han D, Zhang Y, et al. Mechanical properties of auxetic circular and square tubes filled with aluminum foam. *Eng Struct*. 2023;281:115732.
11. Xie J, Xu Y, Meng Z, Liang M, Wan Z, Šavija B. Peanut shaped auxetic cementitious cellular composite (ACCC). *Construct Build Mater*. 2024;419:135539.
12. Linforth S, Ngo T, Tran P, Ruan D, Odish R. Investigation of the auxetic oval structure for energy absorption through quasi-static and dynamic experiments. *Int J Impact Eng*. 2021;147:103741.
13. Lu F, Ling X, Li W, Zhang C, Wei T, Zhu Y. On the in-plane effective elastic constants of a novel anti-tetrachiral meta-structure with L-type ligaments. *Eng Struct*. 2024;303:117550.
14. Li T, Li Y. Effects of handedness ratio and handedness distribution on the mechanical properties of Bi-chiral mechanical metamaterials. *Int J Solids Struct*. 2022;254-255:111947.
15. Hu T, Pan T, Guo D, et al. Omnidirectional configuration of stretchable strain sensor enabled by the strain engineering with chiral auxetic metamaterial. *ACS Nano*. 2023;17:22035-22045.
16. Hu LL, Ye WK, Wu ZJ. Mechanical property of anti-trichiral honeycombs under large deformation along the x-direction. *Thin-Walled Struct*. 2019;145:106415.
17. Lakes RS, Elms K. Indentability of conventional and negative Poisson's ratio foams. *J Compos Mater*. 1993;27(12):1193-1202.
18. Hu LL, Zhou MZ, Deng H. Dynamic indentation of auxetic and non-auxetic honeycombs under large deformation. *Compos Struct*. 2019;207:323-330.
19. Zhang XY, Ren X, Wang XY, et al. A novel combined auxetic tubular structure with enhanced tunable stiffness. *Compos B Eng*. 2021;226.
20. Lakes R. Advances in negative Poisson's ratio materials. *Adv Mater*. 2004;5:293-296.
21. Yang W, Li ZM, Shi W, Xie BH, Yang MB. Review on auxetic materials. *J Mater Sci*. 2004;39:3269-3279.
22. Dykstra DMJ, Lenting C, et al. Buckling metamaterials for extreme vibration damping. *Adv Mater*. 2023;35:e2301747.
23. Li X, Yu X, Zhai W. Additively manufactured deformation-recoverable and broadband sound-absorbing microlattice inspired by the concept of traditional perforated panels. *Adv Mater*. 2021;33:e2104552.
24. Ma L, Chen YL, Yang JS, et al. Modal characteristics and damping enhancement of carbon fiber composite auxetic double-arrow corrugated sandwich panels. *Composite Structures*. 2018;203:539-550.

25. Zeng W, Jiang W, Liu J, Huang W. Fabrication method and dynamic responses of composite sandwich structure with reentrant honeycomb cores. *Compos Struct*. 2022;299:116084.
26. Li J, Wei Y, Wu H, et al. Experimental crushing behavior and energy absorption of angular gradient honeycomb structures under quasi-static and dynamic compression. *Def Technol*. 2024;36:47-63.
27. Qi C, Jiang F, Yu C, Yang S. In-plane crushing response of tetra-chiral honeycombs. *Int J Impact Eng*. 2019;130:247-265.
28. Montazeri A, Saeedi A, Bahmanpour E, Mahnama M. Auxetic mechanical metamaterials with symmetry-broken Re-entrant units. *Int J Mech Sci*. 2024;266:108917.
29. Lang JP, Jiang W, Teng XC, et al. Assembled mechanical metamaterials with transformable shape and auxeticity. *Construct Build Mater*. 2023;378:131181.
30. Han D, Ren X, Zhang Y, et al. Lightweight auxetic metamaterials: design and characteristic study. *Compos Struct*. 2022;293:115706.
31. Li C, Shen HS, Wang H, Yu Z. Large amplitude vibration of sandwich plates with functionally graded auxetic 3D lattice core. *Int J Mech Sci*. 2020;174:105472.
32. Lira C, Scarpa F, Rajasekaran R. A gradient cellular Core for aeroengine Fan blades based on auxetic configurations. *J Intell Mater Syst Struct*. 2011;22:907-917.
33. Hanna B, Adams R, Townsend S, et al. Auxetic metamaterial optimisation for head impact mitigation in American football. *Int J Impact Eng*. 2021;157:103991.
34. Chen Z, Li J, Wu B, Chen X, Ren X, Xie YM. A novel bio-inspired helmet with auxetic lattice liners for mitigating traumatic brain injury. *Smart Mater Struct*. 2023;32:105020.
35. Jiang Y, Liu Z, Matsuhisa N, et al. Auxetic mechanical metamaterials to enhance sensitivity of stretchable strain sensors. *Adv Mater*. 2018;30:e1706589.
36. Hong L, Zhang H, Kraus T, et al. Ultra-stretchable Kirigami piezo-metamaterials for sensing coupled large deformations. *Adv Sci Weinh*. 2023;11:e2303674.
37. Zahed M, Ardeshiri JR, Safarabadi M. Reinforcement of 3D-printed Re-entrant structures using additional supports under three-point bending, experimental and numerical analyses. *Adv Eng Mater*. 2023;26:2301252.
38. Chen Z, Li J, Wu B, Chen X, Min Xie Y. Enhanced mechanical properties of re-entrant auxetic honeycomb with self-similar inclusion. *Compos Struct*. 2024;331:117921.
39. Ni XH, Jiang W, Zhang XG, et al. Quasi-static and dynamic properties studies of a metamaterial with enhanced auxeticity and tunable stiffness. *Compos Struct*. 2023;321:117254.
40. Wang XT, Wang B, Li XW, Ma L. Mechanical properties of 3D re-entrant auxetic cellular structures. *Int J Mech Sci*. 2017;131-132:396-407.
41. Wang XT, Li XW, Ma L. Interlocking assembled 3D auxetic cellular structures. *Mater Des*. 2016;99:467-476.
42. Ma X, Zhang N, Chang Y, Tian X. Multi-step deformation lattice structures from the rotation of unit cell. *Int J Solids Struct*. 2024;288:112599.
43. Etemadi E, Zhang M, Li K, et al. Load-bearing characteristics of 3D auxetic structures made with carbon fiber reinforced polymer composite. *Compos Struct*. 2023;319:117206.
44. Gao Y, Zhou Z, Hu H, Xiong J. New concept of carbon fiber reinforced composite 3D auxetic lattice structures based on stretching-dominated cells. *Mech Mater*. 2021;152:103661.
45. Zhang M, Li K, Ho MMP, et al. Low-velocity impact response of 3D carbon fiber reinforced polymer auxetic lattice structures. *Polym Compos*. 2024;45(8):7191-7204. doi:10.1002/pc.28259
46. Wang XT, Wang B, Wen ZH, Ma L. Fabrication and mechanical properties of CFRP composite three-dimensional double-arrow-head auxetic structures. *Compos Sci Technol*. 2018;164:92-102.
47. Yu S, Liu Z, Cao X, Liu J, Huang W, Wang Y. The compressive responses and failure behaviors of composite graded auxetic re-entrant honeycomb structure. *Thin-Walled Struct*. 2023;187:110721.
48. Li ZY, Wang XT, Ma L, Wu LZ, Wang L. Auxetic and failure characteristics of composite stacked origami cellular materials under compression. *Thin-Walled Struct*. 2023;184:110453.
49. Li ZY, Wang WJ, Ye XD, et al. Mechanical properties of 3D continuous CFRP composite graded auxetic structures. *Construct Build Mater*. 2024;440:137379.
50. Li ZY, Wang XT, Yang JS, et al. Mechanical response and auxetic properties of composite double-arrow corrugated sandwich panels with defects. *Mech Adv Mater Struct*. 2021;29:6517-6529.
51. Li ZY, Zhang WM, Wang WJ, et al. New 3D petal-like structures with lightweight, high strength, high energy absorption, and auxetic characteristics. *Thin Walled Struct*. 2024;205:112483. doi:10.1016/j.tws.2024.112483
52. Li ZY, Zhang WM, Zou S, et al. Quasi-static uniaxial compression and low-velocity impact properties of composite auxetic CorTube structure. *Thin-Walled Struct*. 2024;202:112059.
53. Li ZY, Li HZ, Yang JS, et al. Multifunctional acoustic and mechanical metamaterials prepared from continuous CFRP composites. *Mater Horiz*. 2024;12:458-472.
54. Li ZY, Wang XT, Ma L, Wu LZ. Study on the mechanical properties of CFRP composite auxetic structures consist of corrugated sheets and tubes. *Compos Struct*. 2022;292:115655.
55. Li J, Pokkalla DK, Wang ZP, Wang Y. Deep learning-enhanced design for functionally graded auxetic lattices. *Eng Struct*. 2023;292:116477.
56. Ma B, Cao X, Feng Y, et al. A comparative study on the low velocity impact behavior of UD, woven, and hybrid UD/woven FRP composite laminates. *Compos B Eng*. 2024;271.
57. Yang H, Jiang W, Li M, Ma L. Multi-material 3D double-V metastructures with tailorable Poisson's ratio and thermal expansion. *Int J Mech Sci*. 2021;210:106733.
58. Liu A, Chen Y, Hu J, et al. Low-velocity impact damage and compression after impact behavior of CF/PEEK thermoplastic composite laminates. *Polym Compos*. 2022;43:8136-8151.
59. Li S, Yang JS, Schmidt R, Wu LZ, Schröder KU. Compression and hysteresis responses of multilayer gradient composite lattice sandwich panels. *Marine Struct*. 2021;75:102845.
60. Yuan S, Chua CK, Zhou K. 3D-printed mechanical metamaterials with high energy absorption. *Adv Mater Technol*. 2018;4(3):1800419. doi:10.1002/admt.201800419
61. Hu B, Li M, Jiang J, Zhai W. Development of microcellular thermoplastic polyurethane honeycombs with tailored

elasticity and energy absorption via CO_2 foaming. *Int J Mech Sci*. 2021;197:106324.
62. Salari-Sharif L, Schaedler TA, Valdevit L. Hybrid hollow microlattices with unique combination of stiffness and damping. *J Eng Mater Technol*. 2018;140(3):031003. doi:10.1115/1.4038672
63. Liu W, Song H, Wang Z, Wang J, Huang C. Improving mechanical performance of fused deposition modeling lattice structures by a snap-fitting method. *Mater Des*. 2019;181:108065.
64. Meza LR, Greer JR. Mechanical characterization of hollow ceramic nanolattices. *J Mater Sci*. 2013;49:2496-2508.
65. Zheng X, Smith W, Jackson J, et al. Multiscale metallic metamaterials. *Nat Mater*. 2016;15:1100-1106.
66. Zhang WM, Li ZY, Yang JS, et al. A lightweight rotationally arranged auxetic structure with excellent energy absorption performance. *Mech Mater*. 2022;166:104244.

How to cite this article: Li Z-Y, Wang W-J, Li H-Z, et al. Mechanical properties of novel uniform/gradient auxetic structures made of CFRP composites. *Polym Compos*. 2025;46(12): 10824-10841. doi:10.1002/pc.29656

APPENDIX A

TABLE A1 Mechanical properties of composite laminates made from carbon fiber reinforced orthogonal plain weave fabrics (T300 3 K).

Property	Symbol	Value
Longitudinal Young's modulus	E_{11}, E_{22}	$65GPa$
Out-of-plane modulus	E_{33}	$8.3GPa$
Poisson's ratio	υ_{12}	0.064
Poisson's ratio	$\upsilon_{13}, \upsilon_{23}$	0.32
Shear modulus	G_{12}, G_{13}, G_{23}	$4.2GPa$
Longitudinal tensile strength	X_t	$900MPa$
Longitudinal compressive strength	X_c	$625MPa$
Transverse tensile strength	Y_t	$900MPa$
Transverse compressive strength	Y_c	$625MPa$
Out-of-plane tensile strength	Z_t	$60MPa$
Out-of-plane compressive strength	Z_c	$198MPa$
Shear strength	S_{12}	$118MPa$
Shear strength	S_{13}, S_{23}	$86MPa$
Density	ρ	$1250kg/m^3$

APPENDIX B

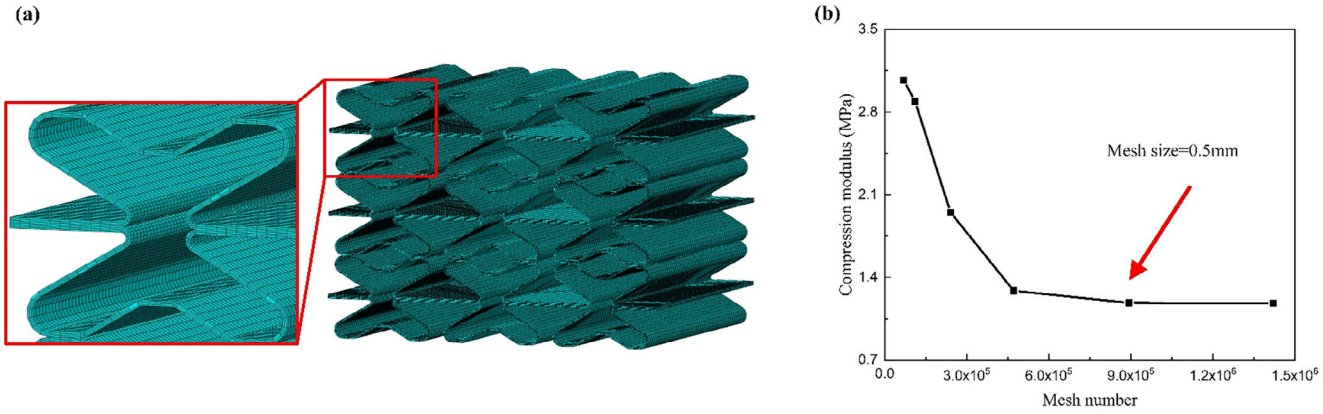

FIGURE A1 Mesh convergence analysis. (A) Meshing details. (B) Mesh convergence.

APPENDIX C

The modified 3D Hashin's failure criterion and Yeh delaminational failure criteria are used into damage initiation model. In composite laminates, five damage modes can be summarized: fiber tensile fracture, fiber compression fracture, matrix tensile fracture, matrix compression fracture and delamination failure. The corresponding five types of failure modes are defined as:

a. Fiber stretching ($\varepsilon_{11} > 0$):

$$R_{ft}^2 = \left(\frac{\varepsilon_{11}}{X_T^\varepsilon}\right)^2 + \left(\frac{\varepsilon_{12}}{S_{12}^\varepsilon}\right)^2 + \left(\frac{\varepsilon_{13}}{S_{13}^\varepsilon}\right)^2 \tag{C.1}$$

b. Fiber compression ($\varepsilon_{11} \le 0$):

$$R_{fc}^2 = \left(\frac{\varepsilon_{11}}{X_C^\varepsilon}\right)^2 \tag{C.2}$$

c. Matrix tension ($\varepsilon_{22} + \varepsilon_{33} \ge 0$):

$$R_{mt}^2 = \left(\frac{\varepsilon_{11}+\varepsilon_{33}}{Y_T^\varepsilon}\right)^2 + \left(\frac{1}{S_{23}^\varepsilon}\right)^2 \left(\varepsilon_{23}^2 - \frac{E_{22}E_{23}}{G_{23}^2}\varepsilon_{22}\varepsilon_{33}\right)^2 + \left(\frac{\varepsilon_{12}}{S_{12}^\varepsilon}\right)^2 + \left(\frac{\varepsilon_{13}}{S_{13}^\varepsilon}\right)^2 \tag{C.3}$$

d. Matrix compression ($\varepsilon_{22} + \varepsilon_{33} < 0$):

$$R_{mc}^2 = \left(\frac{E_{22}\varepsilon_{22} + E_{33}\varepsilon_{33}}{G_{12}S_{12}^\varepsilon}\right)^2 + \left(\frac{\varepsilon_{22}+\varepsilon_{33}}{Y_C^{\varepsilon 2}}\right)\left[\left(\frac{E_{22}Y_C^\varepsilon}{2G_{12}S_{12}^\varepsilon}\right)^2 - 1\right] + \left(\frac{1}{S_{23}^\varepsilon}\right)^2 \left(\varepsilon_{23}^2 - \frac{E_{22}E_{23}}{G_{23}^2}\varepsilon_{22}\varepsilon_{33}\right)^2 + \left(\frac{\varepsilon_{12}}{S_{12}^\varepsilon}\right)^2 + \left(\frac{\varepsilon_{13}}{S_{13}^\varepsilon}\right)^2 \tag{C.4}$$

e. Delamination failure ($\varepsilon_{33} \ge 0$):

$$R_{ld}^2 = \left(\frac{\varepsilon_{33}}{Z_T^\varepsilon}\right)^2 + \left(\frac{\varepsilon_{13}}{S_{13}^\varepsilon}\right)^2 + \left(\frac{\varepsilon_{23}}{S_{23}^\varepsilon}\right)^2 \tag{C.5}$$

where $X_T^\varepsilon, X_C^\varepsilon$ are longitudinal tensile and compressive ultimate strain of composite laminates respectively, $Y_T^\varepsilon, Y_C^\varepsilon$ are transverse tensile and compressive ultimate strain respectively, $S_{23}^\varepsilon, S_{12}^\varepsilon$ and S_{13}^ε are in-plane and out-plane shear ultimate strain respectively, Z_T^ε is tensile delamination ultimate strain. Failure factor $R_i (i = ft, fc, mt, mc, ld)$ represents the failure level. These limit strain components are defined as follows:

$$X_T^\varepsilon = \frac{X_T}{E_{11}},\ X_C^\varepsilon = \frac{X_C}{E_{11}},\ Y_T^\varepsilon = \frac{Y_T}{E_{11}},\ Y_C^\varepsilon = \frac{Y_C}{E_{22}},\ Z_T^\varepsilon = \frac{Z_T}{E_{33}},\ S_{12}^\varepsilon = \frac{S_{12}}{G_{12}},\ S_{13}^\varepsilon = \frac{S_{13}}{G_{13}},\ S_{23}^\varepsilon = \frac{S_{23}}{G_{23}} \tag{C.6}$$

The damage variable d_i is introduced into the damage evolution process to characterize the damage degree of composites. The definition domain of damage variable d_i

is [0,1]. If $d_i = 0$, there is no damage; when $d_i = 1$, the composite material completely lost its mechanical properties. When damage occurs (d_i>0), the corresponding mechanical properties (elastic modulus) begin to deteriorate. The relationship d_i with R_i is shown in Equation (C.7):

$$d_i = \begin{cases} 0 & (R_i < 1) \\ 1 - \dfrac{1}{R_i^m} & (R_i \geq 1) \end{cases}, (i = ft, fc, mt, mc, ld) \tag{C.7}$$

where m (m>0) is the non-dimensional parameter to control the stiffness degradation rate of composite material. At time t, the damage variable as:

$$d_i^t = max\left(d_i^\tau, 0\right), (\tau \leq t; i = ft, fc, mt, mc, ld) \tag{C.8}$$

Based on damage variation, the stress–strain relationship of laminates can be expressed as:

$$\begin{Bmatrix} \varepsilon_{11} \\ \varepsilon_{22} \\ \varepsilon_{33} \\ \gamma_{12} \\ \gamma_{23} \\ \gamma_{13} \end{Bmatrix} = \begin{bmatrix} \dfrac{1}{E_{11}(1-\omega_1)} & -\dfrac{\nu_{12}}{E_{22}} & -\dfrac{\nu_{13}}{E_{33}} & & & \\ -\dfrac{\nu_{12}}{E_{22}} & \dfrac{1}{E_{22}(1-\omega_2)} & -\dfrac{\nu_{23}}{E_{22}} & & 0 & \\ -\dfrac{\nu_{13}}{E_{33}} & -\dfrac{\nu_{23}}{E_{22}} & \dfrac{1}{E_{33}(1-\omega_3)} & & & \\ & & & \dfrac{1}{G_{12}(1-\omega_4)} & 0 & 0 \\ & 0 & & 0 & \dfrac{1}{G_{23}(1-\omega_5)} & 0 \\ & & & 0 & 0 & \dfrac{1}{G_{13}(1-\omega_6)} \end{bmatrix} \begin{Bmatrix} \sigma_{11} \\ \sigma_{22} \\ \sigma_{33} \\ \tau_{12} \\ \tau_{23} \\ \tau_{13} \end{Bmatrix} \tag{C.9}$$

where damage parameter $\omega_i = (i = 1, \cdots, 6)$ is defined as:

$$\begin{aligned} \omega_1 &= max\left(0, d_f\right), \omega_2 = max\left(0, d_f, d_m\right), \omega_3 \\ &= max\left(0, d_f, d_d\right), \omega_4 = max\left(0, d_f, d_m\right), \omega_5 \\ &= max\left(0, d_f, d_d\right), \omega_6 = max\left(0, d_f, d_d\right), d_f \\ &= max\left(0, d_{ft}, d_{fc}\right), d_m = max(0, d_{mt}, d_{mc}), d_d \\ &= max(0, d_{ld}) \end{aligned} \tag{C.10}$$

According to the failure criterion, the unit stiffness will degenerate when a unit fails. Therefore, the maximum strain criterion is applied in the VUMAT subroutine to remove the distorted elements. Furthermore, considering the debonding damage was not the mainly damage models for the present composite Petal-like structures, and the simulation of debonding generally requires vast computing capacity and time, the simulation of the debonding between strips was ignored.